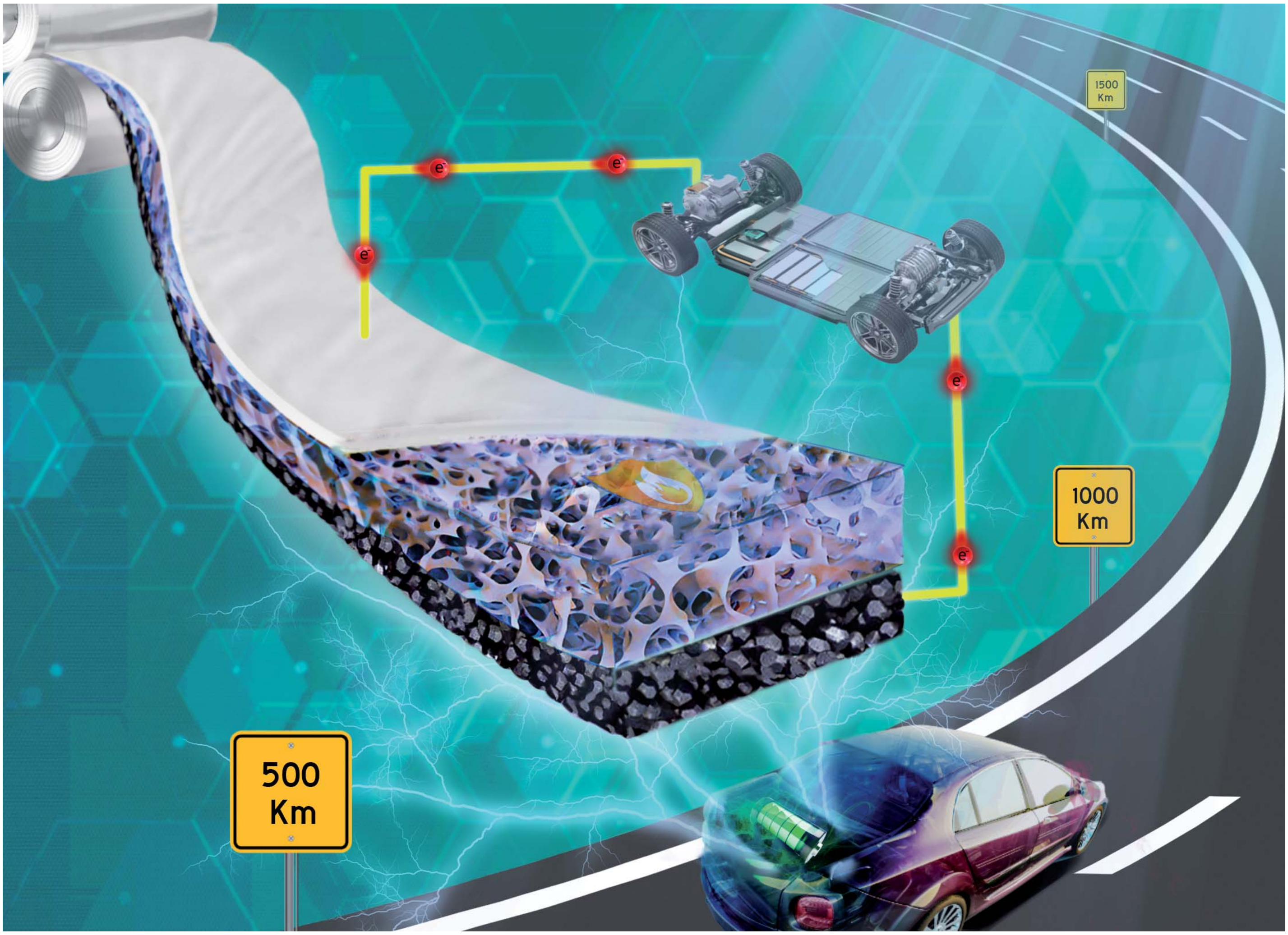

Highlighting a study on solid polymer electrolytes for lithium metal batteries by a group of researchers led by Prof. Hsisheng Teng from National Cheng Kung University.

A scaffold membrane of solid polymer electrolytes for realizing high-stability and dendrite-free lithium-metal batteries

A PVDF-based scaffold membrane reinforces solid polymer electrolytes, extends the applicable voltage, suppresses Li dendrite formation, and enables lithium metal batteries to exhibit high capacities and cycling stability.

As featured in:

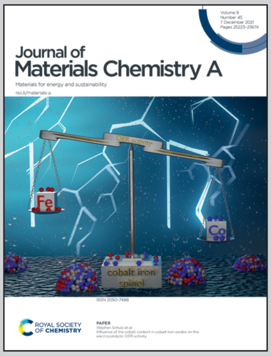
Journal of
Materials Chemistry A

See Hsisheng Teng *et al.*,
J. Mater. Chem. A, 2021, **9**, 25408.

ROYAL SOCIETY
OF **CHEMISTRY**

rsc.li/materials-a

Journal of
Materials Chemistry A

ROYAL SOCIETY
OF CHEMISTRY

PAPER

View Article Online
View Journal | View Issue

Check for updates

Cite this: *J. Mater. Chem. A*, 2021, **9**, 25408

A scaffold membrane of solid polymer electrolytes for realizing high-stability and dendrite-free lithium-metal batteries†

Hanh T. T. Nguyen,[a] Dang H. Nguyen,[a] Qin-Cheng Zhang,[a] Yuh-Lang Lee,[ab] Jeng-Shiung Jan,[a] Chi-Cheng Chiu[a] and Hsisheng Teng*[ab]

Received 11th August 2021
Accepted 7th October 2021

DOI: 10.1039/d1ta06838e

rsc.li/materials-a

High stability and uniform Li deposition are essential for realizing applications of Li-metal batteries (LMBs). Therefore, a scaffold for polymer electrolytes is designed to achieve highly stable operation and dendrite-free Li deposition. A porous membrane of poly(vinylidene fluoride-*co*-hexafluoropropylene) (PVdF-HFP) is synthesized as a scaffold to host a networked poly(ethylene oxide) (PEO)-based solid polymer electrolyte (NSPE) and form a scaffold-hosted electrolyte (NSPE@PF) that exhibits a considerably higher ionic conductivity and Li^+-transference number at 30 °C than the reported PEO-based solid polymer electrolytes do. The PVdF-HFP scaffold renders the NSPE@PF electrochemically stable until 5.4 V (*vs.* Li/Li^+). The PVdF-HFP membrane facilitates uniform Li deposition on both Cu- and Li-metal anodes with negligible dendrite growth in both solid-polymer and liquid electrolyte systems. LMBs containing the NSPE@PF exhibit high capacities and a high cycling stability of up to 1100 cycles. The high-dielectric feature of the PVdF-HFP scaffold facilitates counter-ion-pair dissociation and extends the stable voltage range. Its anion-tethering ability minimizes the space-charge zones on the Li-anode surface and suppresses Li-dendrite growth. Moreover, the high mechanical strength of the scaffold facilitates the synthesis of thin and practically usable NSPE@PFs. This scaffold design is promising for realizing LMB applications.

Introduction

Li-metal batteries (LMBs), in which Li metal is used as the anode, are considered as high-energy storage systems due to their relatively high theoretical capacity (3860 mA h g^{-1}) and low redox potential (−3.04 V *vs.* the standard hydrogen electrode) for Li metal.[1,2] However, the development of practical LMBs is hindered by the high reactivity of metallic Li with liquid electrolytes.[3–5] The interaction between liquid electrolytes and Li metal produces fragile solid electrolyte interface (SEI) materials that inhibit Li-ion transport and cause nonhomogeneous plating on the Li anode, which results in dendrite formation.[6] The pulverization of the fragile SEI by Li dendrites promotes the formation of a new SEI, which reduces the Li content.[7–9] Therefore, the use of solvent-free solid electrolytes has been proposed as an alternative to liquid electrolytes for producing LMBs.

Solid polymer electrolytes (SPEs) are ion-conducting solid materials comprising a solvent-free polymer framework and dissociable Li salts.[10–12] SPEs can help overcome solvent-induced safety issues, including leakage, fire, and explosions. Poly(ethylene oxide) (PEO)-based SPEs have been investigated because of their outstanding ability to form complexes with alkali metal salts.[13] Unfortunately, most PEO-based SPEs have a low ionic conductivity at room temperature,[14] which prevents their practical application. The ionic conductivity of SPEs depends on the local segmental motion of the polymer chains in the amorphous region.[15] Efforts to increase the room-temperature ionic conductivity of SPEs include the addition of nanofillers[16,17] and plasticizers (organic liquid plasticizers,[18,19] low-molecular-weight polymers or oligomers,[20] plastic crystal materials,[21–23] and ionic liquids),[24,25] the blending or copolymerization of SPEs with other polymers,[26–31] and the cross-linking of polymer chains to form a polymeric network.[32–34] In addition to the ionic conductivity, the mechanical, thermal, and chemical stability of PEO-based SPEs must be substantially increased if they are to be employed in practical applications.[35]

Studies have demonstrated the synthesis of promising SPEs by using polyhedral oligomeric silsesquioxane (POSS) to form a network of PEO-based polymers.[36–40] Modifying PEO with poly(propylene oxide) (PPO) reduces the crystallization tendency of PEO.[41] Our previous study demonstrated the

---

[a] *Department of Chemical Engineering, National Cheng Kung University, Tainan 70101, Taiwan. E-mail: hteng@mail.ncku.edu.tw*

[b] *Hierarchical Green-Energy Materials (Hi-GEM) Research Center, National Cheng Kung University, Tainan 70101, Taiwan*

† Electronic supplementary information (ESI) available. See DOI: 10.1039/d1ta06838e

advantages of crosslinking linear chains of a triblock copolymer—poly(polypropylene oxide–ethylene oxide–polypropylene oxide) (P(PO–EO–PO))—by using POSS.[36] Fig. S1a and b† shows the structures of P(PO–EO–PO) and POSS, respectively. The POSS molecule is a Si–O–Si framed cage with Si corners, each of which has a tentacle with an epoxy end. The epoxy ends interact with the amino ends of the P(PO–EO–PO) chains to form a three-dimensional network (Fig. S1c†). Lithium bis(trifluoromethanesulfonyl)imide (LiTFSI) was incorporated into this network to form a networked PEO-based SPE (NSPE).

Li-dendrite formation is one of the most critical issues that must be resolved for using Li-metal anodes in batteries. The uneven deposition of Li and the subsequent growth of dendrites during repeated cycling are ascribed to the presence of space-charge regions near the Li-metal anode.[42,43] Scheme 1a shows that the electric field in the space-charge zones governs Li^+ transport.[44,45] Nonuniform Li^+ transport in the space-charge zones created by expelling anions from the vicinity of the negatively charged Li anode occurs whenever charge distribution on the anode is inhomogeneous.[46–48] As displayed in Scheme 1b, space-charge formation can be suppressed and Li^+ transport can be regulated by tethering anions over the electrolyte, which results in the uniform deposition of Li on the Li-metal surface.[49,50]

In this paper, we propose a conceptual electrolyte design (Scheme 1c) in which the NSPE is incorporated with a porous poly(vinylidene fluoride-*co*-hexafluoropropylene) (PVdF-HFP) scaffold to form a PVdF-HFP-hosted NSPE (*i.e.*, NSPE@PF). The incorporation of PVdF-HFP increased the mechanical stability, chemical stability, and ionic conductivity of the NSPE.[50–54] PVdF-HFP contains polar $–CF_2–$ units on the polymer chains and was reported to induce strong ion–dipole interaction between anions and the polymer,[55] thereby restricting the motion of anions. As illustrated in Scheme 1c, the PVdF-HFP chains tethered the anions to facilitate Li^+ transport. The localization of the anions suppressed the formation of a space-charge zone, which led to uniform Li deposition (Scheme 1b).[49] The mechanically strong PVdF-HFP matrix can also suppress the growth of dendrites that may be formed from some Li-metal nuclei.[56,57] The Li-dendrite formation was considerably lower when using the NSPE@PF than when using the NSPE. An examination of the liquid electrolyte system confirmed the superior function of porous PVdF-HFP in regulating Li^+ deposition. During operation at 30 °C, an all-solid-state LMB, namely Li|NSPE@PF|$LiFePO_4$, exhibited high capacity at a current rate of 0.1C–3C and retained 52% of its original capacity after 1100 charge–discharge cycles at a current rate of 0.3C.

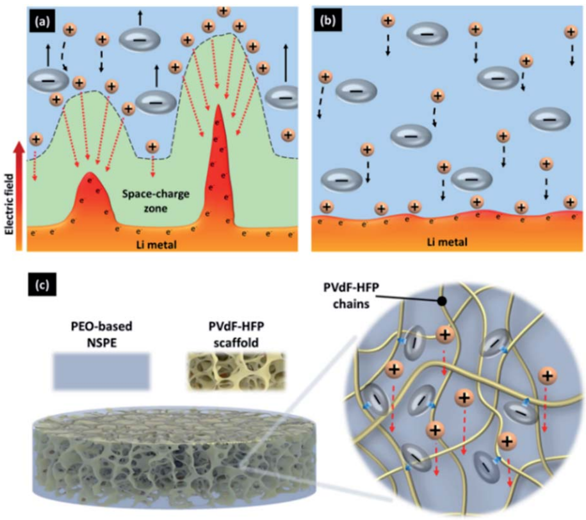

Scheme 1 (a) and (b) Transport patterns of Li ions near the Li-metal anode. (a) Li-dendrite growth due to space-charge zone formation. (b) Uniform Li deposition due to the use of anion tethering for eliminating the space-charge zone. (c) Conceptual design of the NSPE@PF, which consists of a PEO-based NSPE hosted by a poly(vinylidene fluoride-*co*-hexafluoropropylene) (PVdF-HFP) scaffold. The PVdF-HFP polymer chains tether the anions to facilitate Li^+ transport.

Results and discussion

Physical characteristics of NSPE@PF

Solution casting was used to prepare the porous PVdF-HFP membranes. As-purchased PVdF-HFP was dissolved in water–acetone solvent mixtures with varying water contents (1.5–3.0 vol%) to form viscous solutions. These solutions were then coated on a Teflon disk to evaporate the acetone at room temperature. The acetone-evaporated membranes contained water, and the amount of water trapped increased with the water content of the original water–acetone mixture. We placed the membranes in a vacuum oven at 80 °C to remove the trapped water and obtain porous membranes. The structure of the porous membranes was dependent on the amount of trapped water. Fig. S2† displays the top-view scanning electron microscopy (SEM) images of the porous PVdF-HFP membranes, which were denoted as PVdF-HFP-*x*, where *x* is the water content (in vol%) in the water–acetone solvent. The SEM images indicate that pore openings were distributed on the surface of the PVdF-HFP-*x* membranes. The pore size was larger with $x = 1.5$ and 2.5 and smaller with $x = 2.0$ and 3.0. Fig. S3† presents the corresponding side-view SEM images of the PVdF-HFP membranes, showing the *x*-value dependence of porosity consistent with the result obtained from the top-view images. The porosity of the PVdF-HFP-1.5, -2.0, -2.5, and -3.0 membranes was measured to be 40%, 33%, 50%, and 25%, respectively. Both the top- and side-view SEM images depicted the high uniformity of pores in PVdF-HFP-2.5, which may be the reason for the high porosity. The PVdF-HFP-3.0 membrane exhibited shrunken pores (Fig. S2 and S3†) probably because of the collapse of pores in a vacuum during the removal of a large amount of water.

Fig. 1a shows the SEM images of the PVdF-HFP-2.5 membrane, on which pore openings of uniform size were evenly distributed over the surface. Fig. 1b depicts the closeup of a pore opening; a three-dimensional porous network is observed throughout the membrane. Such a scaffold of the PVdF-HFP-2.5 membrane can accommodate the NSPE and reinforce the mechanical strength of the resulting electrolyte. Differential scanning calorimetry (DSC) was performed for

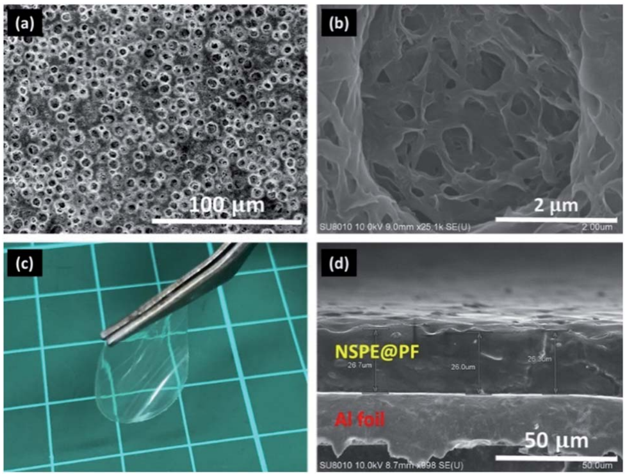

Fig. 1 Surface images of the PVdF-HFP-2.5 and NSPE@PF membranes. (a) Top-view SEM image of PVdF-HFP-2.5. (b) SEM image of a pore opening on the PVdF-HFP-2.5 membrane. (c) Photograph of the NSPE@PF membrane. (d) Side-view SEM image of the NSPE@PF membrane.

analyzing the thermal properties of the PVdF-HFP-2.5 membrane. The range of temperatures scanned was between −100 and 200 °C. Fig. S4a† shows a melting peak appearing at *ca.* 145 °C with a glass transition temperature (T_g) of −20 °C, indicating that the segmental motion of polymer chains would be restricted at low temperatures. Fig. S5† presents the mechanical strength analysis results of the PVdF-HFP-2.5 membrane, which exhibited a high tensile strength. In this study, we used the PVdF-HFP-2.5 membrane as the scaffold for NSPE@PF synthesis because this membrane is highly compatible with the NSPE. Fig. 1c shows that the NSPE@PF membrane was flexible and highly transparent, which reflected the amorphous and homogeneous structure of the membrane. As a comparison, Fig. S6† presents the opaque membrane with the NSPE infiltrated into the PVdF-HFP-1.5 scaffold, which also had high porosity but with an uneven pore distribution (Fig. S2†) to scatter light. The result indicates that this combination did not produce a homogeneous membrane. PVdF-HFP-2.5, with its high porosity and homogeneity, can act as a scaffold to effectively and uniformly accommodate the NSPE.

Fig. 1d displays the side-view SEM image of the NSPE@PF membrane. This membrane was approximately 26 µm thick and had a dense and uniform structure that is favorable for battery assembly. Fig. S7† shows the top-view SEM image of the NSPE@PF membrane, which exhibits a uniform texture distributed with wrinkles resulting from the solvent removal during membrane synthesis.

DSC analysis of the NSPE@PF membrane (Fig. S4a†) shows no melting peaks in the DSC profile, which indicates that the NSPE@PF membrane had low crystallinity. The NSPE@PF membrane exhibited a low glass transition temperature (T_g) of approximately −48 °C, which indicates the high segmental mobility of the polymer chains. Fig. S4a† indicates that the DSC profiles of the NSPE@PF and NSPE membranes were similar, which suggests that the NSPE@PF membrane inherited the thermal properties and behavior of the NSPE. Fig. S8† presents the X-ray diffraction patterns of the NSPE and its precursor P(PO–EO–PO). The pattern of the P(PO–EO–PO) precursor exhibited strong diffraction peaks whereas the peaks of the NSPE were substantially eliminated due to the polymer-networking with the POSS crosslinker, reflecting the low crystallinity of the NSPE. Fig. S4a† depicts a small melting peak at around 20 °C for the NSPE. The incorporation of the PVdF-HFP scaffold further suppressed the formation of crystalline domains in the NSPE, resulting in the absence of a melting signal in the DSC profile of NSPE@PF. The glass-transition and melting peaks of the PVdF-HFP scaffold did not appear in the NSPE@PF profile, indicating that the polymer chains of the NSPE interpenetrated into the PVdF-HFP framework to eliminate the occurrence of both glass-transition and melting in the scaffold. However, a low T_g is detrimental to the mechanical properties of a polymer. The tensile strength of the NSPE@PF membrane was 13 times that of the NSPE because of the reinforcement by the PVdF-HFP scaffold (Fig. S5†), which facilitates facile assembly. We subjected the NSPE@PF, NSPE and PVdF-HFP scaffold membranes to thermogravimetric analysis. The results of this analysis (Fig. S4b†) indicated the high thermal stability of the PVdF-HFP scaffold. The thermal stability of NSPE@PF was retained until approximately 310 °C, which was lower than that of the NSPE (350 °C). The lowered decomposition temperature of NSPE@PF can be attributed to the loss of crystalline domains in the polymer incorporation. Nevertheless, a decomposition temperature of 310 °C is still high for practical applications.

The ion–ion and ion–polymer interactions in the membranes were investigated using Raman spectroscopy in the spectral range of 725–760 cm^{-1}, in which the expansion–contraction mode of the TFSI$^-$ anions was observed.[58] Fig. 2 shows a comparison between the TFSI$^-$ bands observed for the NSPE@PF and NSPE membranes. The TFSI$^-$ band for the NSPE@PF membrane shifted toward a lower wavenumber than that for the NSPE membrane (from 741 to 739 cm^{-1}). This shift can be ascribed to the release of TFSI$^-$ anions from the Li$^+$–TFSI$^-$ ion pairs, in which paired TFSI$^-$ exhibits a higher

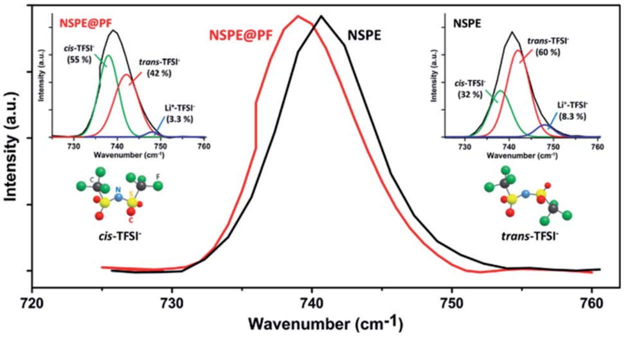

Fig. 2 Raman spectra of the TFSI$^-$ vibration in the NSPE@PF and NSPE at 725–760 cm^{-1}. In the insets, the bands are deconvoluted into three conformers: one free TFSI$^-$ state in the *cis* conformation (738 cm^{-1}), one free TFSI$^-$ state in the *trans* conformation (742 cm^{-1}), and one Li$^+$-associated TFSI$^-$ state (748 cm^{-1}).

wavenumber of 748 cm^{-1}.[59] As displayed in the insets of Fig. 2, the Raman bands were deconvoluted into three conformer peaks by using Gaussian/Lorentzian functions: one free $TFSI^-$ state in the cis conformation (738 cm^{-1}), one free $TFSI^-$ state in the trans conformation (742 cm^{-1}), and one Li^+-associated $TFSI^-$ state (748 cm^{-1}).[60,61] The fractions of Li^+-associated $TFSI^-$ in the entire $TFSI^-$ population were 3.3% and 8.3% for the NSPE@PF and NSPE, respectively, which indicates that the degree of $TFSI^-$ anion association with Li^+ cations decreased due to the presence of the PVdF-HFP scaffold. The electron-withdrawing POSS cages facilitate Li salt dissociation,[62,63] and the degree of Li salt dissociation in the NSPE was high. The porous PVdF-HFP, which had a high dielectric constant of 8.4,[64,65] might have further dissociated the counterion pairs. With regard to the composition of free $TFSI^-$, the NSPE@PF membrane displayed a high contribution of the *cis*-$TFSI^-$ conformation, which has a smaller size than the *trans* conformation and was the favored conformation under immobilization.[66] This result suggested that $TFSI^-$ anions may have been immobilized on the scaffold through their interaction with fluorine-containing functional groups on the PVdF-HFP chains.

Electrochemical analysis

The ionic conductivity (σ) of the NSPE@PF and NSPE membranes was determined by performing electrochemical impedance spectroscopy (EIS) on a sample inserted between stainless-steel (SS) foils at temperatures of 20–90 °C. Fig. S9† presents the EIS data and the method employed to calculate the ionic conductivities. Fig. 3a shows the temperature (T) dependence of σ in a plot of log(σ) *versus* the reciprocal of T. At 30 °C, the NSPE@PF had a σ value of 1.1×10^{-4} S cm^{-1}, which was higher than the σ value of the NSPE (9.3×10^{-5} S cm^{-1}) and those reported for PEO-based SPEs ($\sim 10^{-6}$ to 10^{-8} S cm^{-1}) (see Table S1†). The high ionic conductivity of the NSPE@PF can be attributed to the incorporation of the PEO-based backbone (P(PO–EO–PO) here) with POSS and PVdF-HFP, which increased the proportion of amorphous domains and facilitated salt dissociation. The ionic conductivity of the NSPE@PF increased with temperature, reaching a high value of 1.0×10^{-3} S cm^{-1} at 90 °C, which indicates that the membrane is suitable for use at high temperatures. The relationship between σ and temperature was not linear (Fig. 3a), which indicates that the ion-hopping-associated Arrhenius equation is inadequate for describing the ion transport behavior in the electrolytes. Fig. 3b displays the fitting of the σ values to the Vogel–Tamman–Fulcher (VTF) model, which is expressed as follows:[67–69]

$$\sigma = A_0 T^{\frac{-1}{2}} \exp\left[-\frac{E_a}{R(T - T_0)}\right]$$

where A_0 is a constant proportional to the number of carrier ions, E_a is the pseudo-activation energy related to the motion of the polymer segmental mobility, T_0 is the ideal glass transition temperature, and R is the gas constant. The VTF model relates the ion transport to the segmental motion of polymer chains in the amorphous zones.[70–72] Fig. 3b displays a linear fit, which indicates that the segmental motion of the polymer chains influenced the ion transport through hopping and/or diffusion. The E_a value for the NSPE@PF was calculated to be 2.9 kJ mol^{-1} (or 0.03 eV), which is lower than the values reported for PEO-based SPEs (~0.5 eV).[73] The low E_a value of the NSPE@PF was ascribed to the high degree of ion-pair dissociation in the electrolyte, which results in low energy barriers to ion transport.

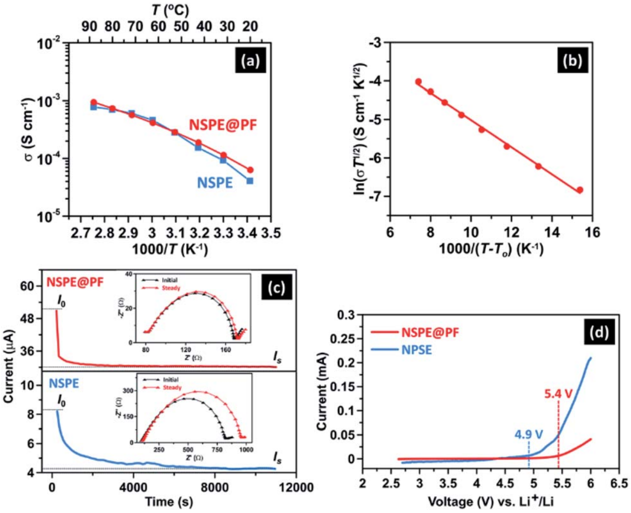

Fig. 3 Electrochemical characteristics of the NSPE@PF and NSPE membranes. (a) Temperature (T) dependence of ionic conductivity (σ) at temperatures of 20–90 °C in a plot of log(σ) *versus* the reciprocal of T. (b) Dependence of ionic conductivity on temperature (T) for NSPE@PF in a plot drawn according to the VTF model. (c) Variations in the current and impedance with time for the symmetric Li|NSPE@PF|Li and Li|NSPE|Li cells under polarization at 10 mV and 30 °C. (d) Linear sweep voltammograms of the NSPE@PF and NSPE assembled in Li||SS cells starting from the open circuit potential (~2.5 V) at a sweep rate of 0.5 mV s^{-1}.

The Li-ion transference number (t_{Li^+}) is an indicator of the Li^+-transport contribution to the ionic conductivity of electrolytes.[74] The t_{Li^+} values of the NSPE@PF and NSPE were determined by substituting the currents and resistances measured during the polarization (ΔV, 10 mV) of a symmetric Li|NSPE@PF|Li cell in the following equation:[75]

$$t_{Li^+} = \frac{I_s(\Delta V - I_0 R_0)}{I_0(\Delta V - I_s R_s)}$$

where I_0 and I_s are the initial and stabilized currents, respectively, under polarization and R_0 and R_s are the corresponding interfacial resistances measured using EIS. Fig. 3c shows the variations in current under polarization and the initial and stabilized EIS impedance spectra (inset) of the Li|NSPE@PF|Li and Li|NSPE|Li cells at 30 °C. The t_{Li^+} value of the NSPE@PF was calculated to be 0.45, which is significantly higher than the values reported for PEO-based SPEs (0.2–0.3) and carbonate-based LEs (0.3–0.4) (Table S1†). The t_{Li^+} value of the NSPE was determined to be 0.32, which was lower than that of NSPE@PF. The high t_{Li^+} value of NSPE@PF supports the interpretation obtained from the Raman analysis, which suggests that the NSPE@PF may have restricted the motion of $TFSI^-$ anions.

The electrochemical window of the NSPE@PF and NSPE membranes was tested by performing linear sweep voltammetry on Li||SS cells at a sweep rate of 0.5 mV s^{-1}. We did not apply any contact-improving modification on the SS because of the excellent contact between the polymer electrolytes and SS.[76] Fig. 3d indicates that the oxidation potentials of the NSPE@PF and NSPE remained stable until 5.4 and 4.9 V (*vs.* Li/Li$^+$), respectively. The anodic decomposition potential of most oligoether-based SPEs is within the lithiation–delithiation range of most cathode materials, which suggests that the oxidation of SPEs on cathode surfaces is a cause for concern.[77–80] The high decomposition potential of the NSPE@PF can be attributed to the affinity of the high-polarity and high-stability PVdF-HFP toward the electrode and the immobilization of TFSI$^-$ (as indicated by the Raman results and high value of t_{Li^+}), which inhibited the oxidation reactions of the polymer chains and anions. In addition, the NSPE did not contain reactive terminal –OH groups, which were commonly present in PEO materials,[81] and other terminal groups were minimized through crosslinking (see Fig. S1†). The backbone of the NSPE was P(PO–EO–PO), rather than PEO, and the high stability and low surface energy of the –CH$_3$ pendants on the PO segments would be exploited to form stable contact with the electrodes. The high electrochemical stability of the NSPE@PF demonstrates its feasibility for use in practical applications.

Regulated Li deposition with PVdF-HFP

Fig. 4a displays the galvanostatic Li plating/stripping profiles of symmetric Li||Li cells with the NSPE and NSPE@PF at different current densities. The electrodes of the cells were alternately plated and stripped with Li, with each plating and stripping step being performed for 1 h. The Li|NSPE@PF|Li cell exhibited lower Li plating/stripping polarization than the Li|NSPE|Li cell did. Fig. S10a† presents the complex-plane impedance spectra of the Li|NSPE@PF|Li and Li|NSPE|Li cells. The high-frequency semicircle shown in the spectra characterizes the motion of Li$^+$ ions across the Li–SPE interface. The diameter of the semicircle corresponds to the interfacial charge transfer resistance, which was much smaller for the Li|NSPE@PF|Li cell. This impedance analysis demonstrated that the PVdF-HFP scaffold effectively regulated the Li$^+$-ion motion for fluent Li plating/stripping. Following varying-current cycling analysis, the cells were further cycled at 100 μA cm^{-2} for 400 h (Fig. 4b). The Li|NSPE@PF|Li cell exhibited a stable cycling profile, whereas the Li|NSPE|Li cell exhibited considerable voltage fluctuation during cycling and a decline in the polarization overpotential. This result of the Li|NSPE|Li cell indicates that the formation of Li dendrites and dead Li reduced the overpotential. Fig. S10b† presents the Li plating/stripping profiles of the Li|NSPE@PF|Li and Li|NSPE|Li cells obtained at 200 μA cm^{-2}. The Li|NSPE|Li cell exhibited profile fluctuation at this high current and was short-circuited in 4 h, whereas the Li|NSPE@PF|Li cell remained stable at this current, reflecting again the ability of the scaffold in stabilizing Li deposition to prevent cell failure.

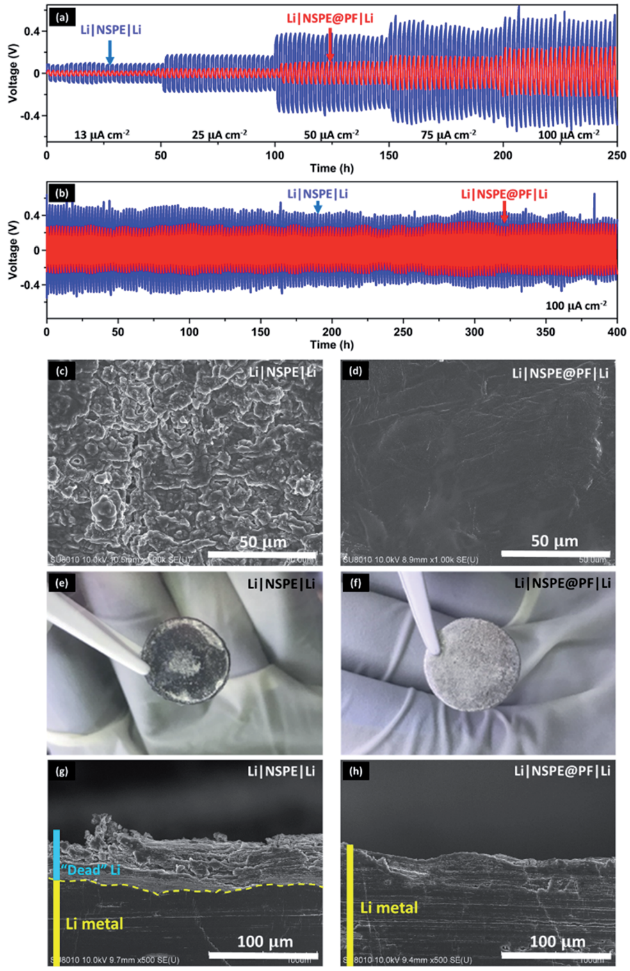

Fig. 4 Cyclic Li plating/stripping profiles of the Li|NSPE@PF|Li and Li|NSPE|Li cells. (a) Voltage profiles at different current densities (0.013–0.1 mA cm^{-2}). (b) Voltage profiles at 0.1 mA cm^{-2} for 400 h. (c) and (d) Top-view SEM images of Li electrodes of the Li|NSPE|Li and Li|NSPE@PF|Li cells after cycling. (e) and (f) Optical images of the Li electrodes of the Li|NSPE|Li and Li|NSPE@PF|Li cells. (g) and (h) Side-view SEM images of the Li electrodes of the Li|NSPE|Li and Li|NSPE@PF|Li cells. The cells were alternately subjected to Li plating and stripping, with each plating and stripping step being performed for 1 h.

Fig. 4c and d shows the top-view SEM images of the Li electrodes of the Li|NSPE|Li and Li|NSPE@PF|Li cells after cycling. Extensive Li-dendrite formation was observed on the electrode of the Li|NSPE|Li cell, whereas smooth and homogenous Li deposition was observed on the electrode of the Li|NSPE@PF|Li cell. The optical image of the Li electrode of the Li|NSPE|Li cell (Fig. 4e) exhibits a dark color, which indicates the rupture of the deposited Li and the formation of dead Li. By contrast, the Li electrode of the Li|NSPE@PF|Li cell exhibits a silver color similar to that of pristine Li metal (Fig. 4f), which indicates stable and uniform Li deposition in the NSPE@PF cell. Fig. 4g and h depicts the side-view SEM images of the Li electrodes. A thick dendritic-Li/dead-Li layer was observed at the electrode interface of the Li|NSPE|Li cell (Fig. 4g), whereas a dense, uniform layer was observed at the interface of the Li|NSPE@PF|Li cell (Fig. 4h). Porous PVdF-HFP may have played a crucial role in suppressing Li-dendrite formation.

To further elucidate the role of the porous PVdF-HFP membrane in hindering Li-dendrite growth, we tested the membrane in an asymmetric Li||Cu cell with a conventional liquid electrolyte of 1 M $LiPF_6$ carbonate solution (LE). For comparison, both LE-soaked PVdF-HFP and commercial Celgard membranes (LE@PF and LE@Celgard, respectively) were inserted in the Li||Cu cell to investigate the Li-plating pattern on the Cu electrode. The Cu electrode was plated with Li at 1 mA in both cells. Fig. 5a and b displays the top-view and side-view images of 1 mA h cm^{-2} Li deposited on the Cu electrode in the Li|LE@Celgard|Cu cell. The top-view image (Fig. 5a) exhibits a fragile structure comprising needle-like dendrites, which may further grow and penetrate the Celgard membrane or crack during stripping to form dead Li. The corresponding side-view image (Fig. 5b) indicates the presence of a thick, loose layer of deposited Li. By contrast, the top-view image of the Li deposit in the Li|LE@PF|Cu cell (Fig. 5c) reveals that Li metal was deposited as granules that grew horizontally and had rounded corners. The corresponding side-view image (Fig. 5d) indicates the existence of a compact layer of deposited Li metal. Fig. S11† presents the plating/stripping test results of LE@PF and LE@Celgard in symmetric Li||Li cells, showing that the Li|LE@PF|Li cell exhibited stable cycling performance for 700 h whereas the Li|LE@Celgard|Li cell short-circuited after 240 h. The comparison between the PVdF-HFP and Celgard membranes indicated that PVdF-HFP effectively regulated Li-ion transport for achieving homogeneous Li deposition on the Cu electrode. This function of porous PVdF-HFP renders it suitable for use in practical LMBs.

Li|LE@PF|$LiFePO_4$ and Li|LE@Celgard|$LiFePO_4$ batteries were assembled to investigate the effectiveness of the PVdF-HFP membrane as a separator in LMBs. These batteries were subjected to charge–discharge cycles at a current rate of 1C at room temperature. As shown in Fig. 6, the Li|LE@PF|$LiFePO_4$ battery exhibited remarkably high cycling stability. It exhibited a discharge capacity of 143 mA h g^{-1} during the first cycle and maintained 91% of its original capacity after 500 cycles with a coulombic efficiency close to 100%. By contrast, the Li|LE@Celgard|$LiFePO_4$ battery exhibited a considerable decrease in discharge capacity and retained only 73% of its original capacity after 500 cycles with a coulombic efficiency of approximately 95%. Thus, the PVdF-HFP membrane is an efficient polymer membrane to minimize the SEI formation, which consumes Li and lowers the coulombic efficiency, and to increase the capacity retention.

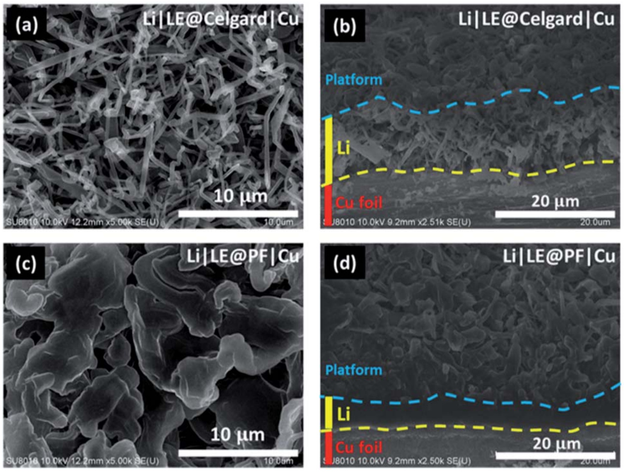

Fig. 5 SEM images of the 1 mA h cm^{-2} Li deposit on the Cu electrodes of Li|LE@PF|Cu and Li|LE@Celgard|Cu cells. (a) Top-view image of the deposited Li in the Li|LE@Celgard|Cu cell. (b) Side-view image of the deposited Li in the Li|LE@Celgard|Cu cell. (c) Top-view image of the deposited Li in the Li|LE@PF|Cu cell. (d) Side-view image of the deposited Li in the Li|LE@PF|Cu cell. The current density was 1.0 mA cm^{-2}, and the deposition time was 1 h.

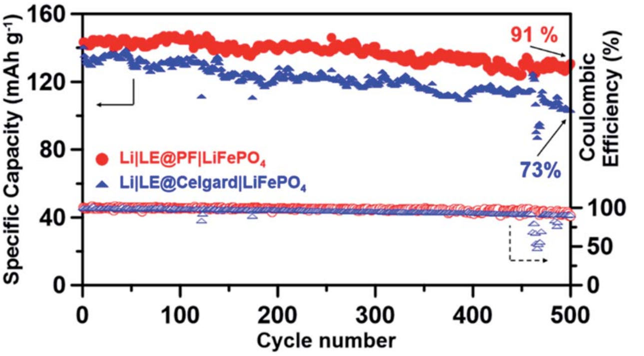

Fig. 6 Cycling performance of the Li|LE@PF|$LiFePO_4$ and Li|LE@Celgard|$LiFePO_4$ batteries under 1C charge–discharge at room temperature.

Performance of solid-state LMBs

The NSPE@PF membrane was incorporated into a Li||$LiFePO_4$ battery to investigate its performance in LMBs. Fig. 7a shows the charge–discharge profiles of the Li|NSPE@PF|$LiFePO_4$ battery, which was charged at a current rate of 0.1C and discharged at different C-rates in the voltage range of 2.5–4.0 V. The battery delivered a high capacity of 164 mA h g^{-1} at a low discharge rate of 0.1C and can be operated at a high rate of 3C.

The polarization of the Li|NSPE@PF|$LiFePO_4$ battery during discharging, the voltage difference between the charge and discharge profiles, is lower than the corresponding values presented in the literature.[34,82,83] The polarization resistance is governed by the ionic conductivity of the electrolyte bulk and the interfacial resistance between the electrode and the electrolyte.[84] This resistance plays a crucial role in maintaining cell stability during charge–discharge cycles.[85]

We subjected the Li|NSPE@PF|$LiFePO_4$ battery to a long-term cycling test between 2.5 and 4.0 V at a current rate of 0.3C. Fig. 7b displays the performance of the Li|NSPE@PF|$LiFePO_4$ battery during cycling. This battery retained 52% of its capacity after 1100 cycles, with the coulombic efficiency remaining approximately 100% throughout the entire cycling duration. Fig. 7c illustrates the charge–discharge profiles of the Li|NSPE@PF|$LiFePO_4$ battery for different numbers of cycles. Only a small increase in polarization was observed during cycling because of stable Li deposition. By contrast, the Li|NSPE|$LiFePO_4$ battery exhibited a high capacity decay after 100 cycles, with a large fluctuation in the coulombic efficiency (Fig. 7b). Fig. S12† shows the charge–discharge profiles of the Li|NSPE|$LiFePO_4$ battery for different

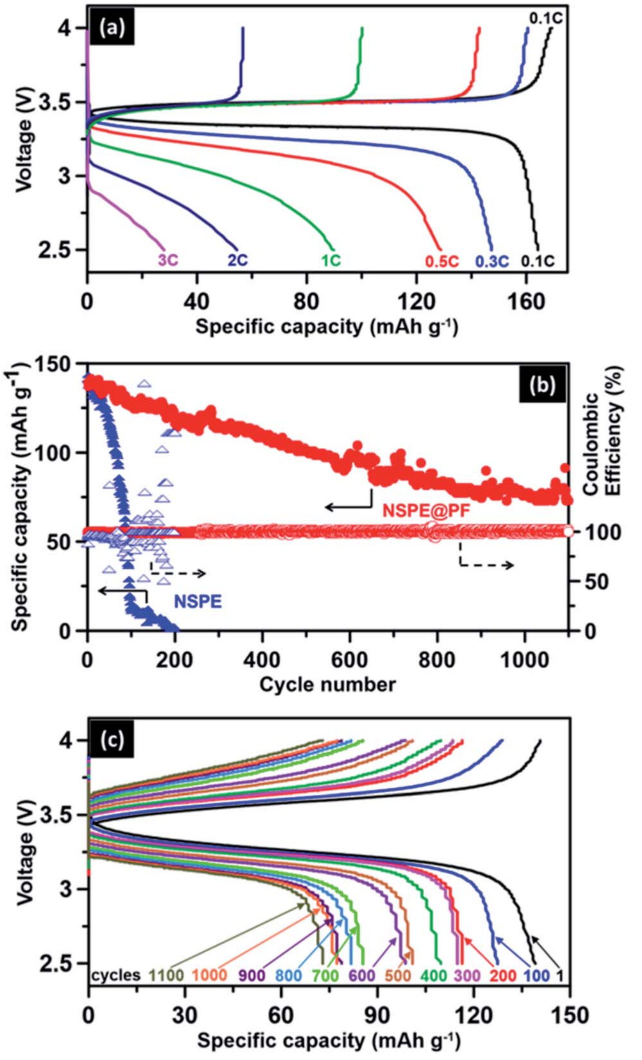

Fig. 7 Electrochemical performance of the Li||$LiFePO_4$ battery at 30 °C. (a) Charge–discharge profiles of the Li|NSPE@PF|$LiFePO_4$ battery, which was charged at 0.1C and discharged at different C-rates within 2.5–4.0 V. (b) Cycling performance of the Li|NSPE@PF|$LiFePO_4$ and Li|NSPE|$LiFePO_4$ batteries charged and discharged at 0.3C within 2.5–4.0 V. (c) Charge–discharge profiles of the Li|NSPE@PF|$LiFePO_4$ battery for different numbers of cycles at 0.3C.

numbers of cycles. A substantial increase in polarization was observed during cycling for this battery. Li dendrites may have formed in the NSPE battery and increased the thickness of the deposited Li layer during cycling, thereby increasing polarization and dead-Li formation and causing substantial capacity decay.

Fig. S13a† presents the impedance spectra of the Li|NSPE@PF|$LiFePO_4$ and Li|NSPE|$LiFePO_4$ batteries to elucidate the interfacial charge transfer resistances. The Li|NSPE@PF|$LiFePO_4$ battery exhibited a smaller high-frequency semicircle than did the Li|NSPE|$LiFePO_4$ battery, corroborating that the scaffold lowered the interfacial resistance. Fig. S13b† presents the impedance spectra of the symmetric $LiFePO_4$||$LiFePO_4$ cells assembled using the NSPE@PF and NSPE. The NSPE@PF resulted in a low resistance (*i.e.*, a small semicircle), indicating that the scaffold facilitated Li^+-ion transfer at the cathode–electrolyte interface. The comparison of the spectra of the symmetric $LiFePO_4$||$LiFePO_4$ (Fig. S13b†) and Li||Li (Fig. S10a†) cells reveals a higher resistance at the Li–SPE interface relative to that at the cathode–SPE. The interfacial resistance of the batteries (Fig. S13a†), which exhibited resistance values between those of the symmetric cells, supported this finding. Further studies to improve the charge transfer resistance between Li and the NSPE@PF are needed for realizing the application of SPEs in LMBs.

As to the elimination of a space-charge zone, we have conducted AC impedance analysis of the Li|NSPE@PF|SS and Li|NSPE|SS cells at different potentials to analyze the interfacial capacitive behavior. Fig. S14a† presents the impedance spectra of the Li|NSPE|SS cell. The spectra exhibited an incomplete semicircle contour at high frequencies and then transformed into a sloping line. A semicircle is characteristic of a pair of parallel capacitance and resistance elements and the sloping line corresponds to a capacitance element for double layer formation on the fractal surface. The inset of Fig. S14a† presents the corresponding equivalent circuit, where R_s is the electrolyte resistance, C_i and R_i are the interfacial capacitance and resistance, and C_d is the double layer capacitance. If the semicircle was simply contributed by the contact between the electrolyte and metal electrodes, the variation of the semicircle shape with the applied potential, as observed in Fig. S14a,† would not occur. The result shown in Fig. S14a† indicated the presence of space-charge zones at the interfaces of the Li|NSPE|SS cell. As can be seen in Fig. S14b†, with the introduction of the PVdF-HFP scaffold, the Li|NSPE@PF|SS cell prevented the semicircle counter to appear in the impedance spectra, indicating that the scaffold prevented the formation of the interfacial space-charge zone.

The developed NSPE@PF membrane effectively expedited and regulated Li^+ transport and allowed Li to be plated uniformly on the Li-metal anodes. This phenomenon occurred because of the combination of the networked polymeric framework and interpenetration with PVdF-HFP, which dissociated ion pairs and tethered $TFSI^-$ anions. This combination increased the mechanical strength, expedited ion transport, and regulated Li^+ flow in the NSPE. The interpenetration between P(PO–EO–PO) and PVdF-HFP chains strengthened the framework and suppressed the crystallization tendency of the polymer. $TFSI^-$-tethered PVdF-HFP eliminated the space-charge zone on the anode surface (Scheme 1a) and regulated the Li^+ flux, thus inhibiting the growth of Li dendrites (Scheme 1b). Fig. 5 indicates that a considerable difference existed between the highly stable Li layer deposited on the Cu anode in the LE entrapped in PVdF-HFP (Fig. 5a) and the thick and fractured deposition layer comprising needle-like Li dendrites in the LE entrapped in a commercial Celgard separator (Fig. 5b).

Conclusions

In this study, we synthesized an all-solid-state electrolyte, NSPE@PF, by using a PVdF-HFP scaffold membrane to accommodate the NSPE, which is an electrolyte with POSS-networked P(PO–EO–PO). The scaffold membrane exhibited high mechanical integrity and reinforced the NSPE to partition firmly the electrodes of an LMB. The PVdF-HFP scaffold facilitated ion-pair dissociation and tethered $TFSI^-$ anions in the NSPE@PF, which resulted in a high ionic conductivity and $t_{Li}{}^+$ value. The NSPE@PF was electrochemically stable until a voltage of 5.4 V (*vs.* Li/Li^+) due to the $TFSI^-$-tethering characteristics and high-dielectric characteristics of PVdF-HFP. The PVdF-HFP membrane minimized the space-charge zone near the electrolyte–anode interface, which resulted in uniform and dendrite-free Li deposition in both SPE- and LE-based LMBs. The resulting all-solid-state Li|NSPE@PF|$LiFePO_4$ battery had a discharge capacity of 164 mA h g^{-1} at 30 °C and retained 52% of its initial capacity after 1100 cycles of charge and discharge at a current rate of 0.3C. This paper presents a promising scaffold design for SPEs and LEs to realize the high-voltage and dendrite-free operation of LMBs.

Experimental

Materials

PVdF-HFP ($M_w = 400\,000$ g mol^{-1}), P(PO–EO–PO) ($M_w = 2000$ g mol^{-1}), the LiTFSI salt for the synthesis of the SPE, the PVdF binder ($M_w = 534\,000$ g mol^{-1}), and the acetonitrile (ACN) solvent were purchased from Sigma-Aldrich, USA. The POSS crosslinking agent (EP0409M_w; 1337.88 g mol^{-1}) was purchased from Hydrid, USA. The $LiFePO_4$ cathode material was purchased from BTR New Energy Materials, China. The conducting agents (Super-P and KS4) were purchased from Taiwan Maxwave Co., Taiwan. *N*,*N*-Dimethylacetamide (DMAc) and acetone were purchased from Alfa Aesar, USA. Commercial Celgard 2325 with a thickness of 15 μm was purchased from Ubiq, Taiwan. P(PO–EO–PO) and LiTFSI were stored in an Ar-filled glovebox.

Material synthesis

The PVdF-HFP membranes were prepared through solution casting. First, as-received PVdF-HFP was dissolved in water-containing acetone solvents. The concentration of PVdF-HFP was fixed at 4.0 wt% in acetone, with the water content of the solutions ranging from 1.5 to 3.0 vol%. Subsequently, 0.6 mL of the solution was coated on a Teflon disk, which allowed the acetone to evaporate slowly at room temperature. After evaporation of acetone, the films were peeled off and placed in a vacuum oven at 80 °C for 12 h to remove the water and obtain PVdF-HFP membranes.

For NSPE synthesis, P(PO–EO–PO) and POSS (at a molar ratio of 12 : 1) were dissolved in ACN in a glovebox at 50 °C for 4 h to form a crosslinked network. After the reaction, LiTFSI was added to the solution at a Li^+ : EO ratio of 1 : 15. The solution was stirred until complete dissolution of the salt to obtain an NSPE-containing solution. Then, the solution was cast on a Teflon disk and kept at 90 °C for 4 h under vacuum to completely remove ACN. The NSPE with a thickness of 50–70 μm was used for the battery tests.

For NSPE@PF synthesis, the PVdF-HFP membranes were immersed in the NSPE-containing solution. The NSPE-containing PVdF-HFP membranes were dried under vacuum at 90 °C for 4 h to completely remove the solvent and obtain the PVdF-HFP-infiltrated NSPE, namely NSPE@PF, which had a thickness of 26 μm.

To fabricate the $LiFePO_4$ cathode, we prepared a mixture of 70 wt% $LiFePO_4$, 15 wt% binder, and 15 wt% conducting agent (Super-P and KS4). This mixture was stirred in DMAc to form a homogeneous slurry. The binder and conducting agent comprised PVdF and NSPE in a weight ratio of 1 : 2, respectively, and Super-P and KS4 in a weight ratio of 2 : 1, respectively. The prepared slurry was coated on Al foil by using a doctor blade. The coated $LiFePO_4$ was dried at 90 °C for 24 h under vacuum. The $LiFePO_4$ loading of the cathodes was approximately 1.7 mg cm^{-2}.

Material characterization

The porosity (ρ) of the PVdF-HFP scaffold was determined according to the following equation:

$$\rho = \frac{\Delta V_{\text{water}} - \Delta V_{\text{ethanol}}}{\Delta V_{\text{water}}} \times 100\%$$

where ΔV_{water} and $\Delta V_{\text{ethanol}}$ are the volume increases of the deionized water and ethanol, respectively, after the PVdF-HFP scaffold was immersed in the two liquids.

The morphology of the SPEs was investigated using a SEM (JEOL JSM-6700F, Japan). The thermal properties were characterized using a DSC (Shimadzu, DSC-60, Japan) and a thermogravimetric analyzer (PerkinElmer, TGA-7, USA). DSC was conducted at a constant heating rate of 10 °C min^{-1} under a continuous N_2 purge. Thermogravimetric analysis was conducted under an N_2 atmosphere from 50 to 800 °C at a heating rate of 10 °C min^{-1}. The mechanical strength of materials was measured using a dynamic mechanical analyzer (TA Instruments, RSA-G2, USA). The Raman spectra of the SPEs were recorded using a BaySpec Raman spectrometer (USA) with a laser line of 780 nm and a resolution of 4 cm^{-1} at room temperature. Gaussian or Lorentzian functions were used to deconvolute the bands of the Raman spectra.

Electrochemical analysis

The ionic conductivities of the SPEs were determined using EIS with a perturbation amplitude of 10 mV and alternating current frequency ranging from 1 MHz to 1 Hz over a temperature range of 20–90 °C. The SPEs were inserted between a pair of SS electrodes in the analysis. Chronoamperometry and EIS analyses were performed using symmetric Li||Li cells to test the Li^+ ion transference number ($t_{Li}{}^+$) of the SPEs. The electrochemical stability window of the SPEs was determined using linear sweep voltammetry, in which scans were conducted for Li||SS cells from the open circuit potential to 6 V (*vs.* Li/Li^+) at 0.5 mV s^{-1}. Symmetric Li||Li cells were used to investigate the performance of Li plating/stripping on the Li anode. Li||$LiFePO_4$ coin cells were assembled to analyze the performance of the SPEs in LMBs. The interfacial capacitive behavior of the SPEs was analyzed using AC impedance spectroscopy on the Li||SS cells, which were analyzed at different potentials (1.6–2.4 V (Li/Li$^+$)) with an AC amplitude of 10 mV and a frequency range of 100 kHz to 0.1 Hz.

Author contributions

H. T. T. N.: conceptualization, data curation, formal analysis, investigation, methodology, writing – original draft, writing – review & editing. D. H. N.: data curation, formal analysis. Q. C. Z.: data curation, formal analysis. Y. L. L., J. S. J., C. C. C.: methodology, validation. H. T.: funding acquisition, project administration, resources, supervision, validation, investigation, writing – original draft, writing – review & editing.

Conflicts of interest

There are no conflicts to declare.

Acknowledgements

The authors acknowledge the support of The Ministry of Science and Technology in Taiwan through grant numbers 109-2923-E-006-006, 109-2622-8-006-005, 108-3116-F-006-012-CC1, and 108-2622-8-006-014. The authors also acknowledge the support from the Hierarchical Green-Energy Materials (Hi-GEM) Research Center and the Center of Applied Nanomedicine at National Cheng Kung University from The Featured Areas Research Center Program within the framework of the Higher Education Sprout Project by the Ministry of Education and the Ministry of Science and Technology (109-2634-F-006-020).

References

1 X.-B. Cheng, R. Zhang, C.-Z. Zhao and Q. Zhang, *Chem. Rev.*, 2017, **117**, 10403.
2 Z. A. Ghazi, Z. Sun, C. Sun, F. Qi, B. An, F. Li and H. M. Cheng, *Small*, 2019, **15**, 1900687.
3 W. Xu, J. Wang, F. Ding, X. Chen, E. Nasybulin, Y. Zhang and J.-G. Zhang, *Energy Environ. Sci.*, 2014, **7**, 513.
4 J.-M. Tarascon and M. Armand, *Nature*, 2011, 171.
5 Y. Lu, Z. Tu and L. A. Archer, *Nat. Mater.*, 2014, **13**, 961.
6 Y. Liu, D. Lin, P. Y. Yuen, K. Liu, J. Xie, R. H. Dauskardt and Y. Cui, *Adv. Mater.*, 2017, **29**, 1605531.
7 W. Zhang, H. L. Zhuang, L. Fan, L. Gao and Y. Lu, *Sci. Adv.*, 2018, **4**, eaar4410.
8 M. Rosso, T. Gobron, C. Brissot, J.-N. Chazalviel and S. Lascaud, *J. Power Sources*, 2001, **97**, 804.
9 R. Zhang, X. Shen, X.-B. Cheng and Q. Zhang, *Energy Storage Mater.*, 2019, **23**, 556.
10 L. Long, S. Wang, M. Xiao and Y. Meng, *J. Mater. Chem. A*, 2016, **4**, 10038.
11 W. H. Meyer, *Adv. Mater.*, 1998, **10**, 439.
12 J. Lopez, D. G. Mackanic, Y. Cui and Z. Bao, *Nat. Rev. Mater.*, 2019, **4**, 312.
13 Y. Zhao, Y. Bai, W. Li, M. An, Y. Bai and G. Chen, *Chem. Mater.*, 2020, **32**, 6811.
14 Y. Zheng, Y. Yao, J. Ou, M. Li, D. Luo, H. Dou, Z. Li, K. Amine, A. Yu and Z. Chen, *Chem. Soc. Rev.*, 2020, **49**, 8790.
15 Z. Xue, D. He and X. Xie, *J. Mater. Chem. A*, 2015, **3**, 19218.
16 J. Weston and B. Steele, *Solid State Ionics*, 1982, **7**, 75.
17 D. Lin, W. Liu, Y. Liu, H. R. Lee, P.-C. Hsu, K. Liu and Y. Cui, *Nano Lett.*, 2016, **16**, 459.
18 H. Pitawala, M. Dissanayake, V. Seneviratne, B.-E. Mellander and I. Albinson, *J. Solid State Electrochem.*, 2008, **12**, 783.
19 L. Fan, Z. Dang, C.-W. Nan and M. Li, *Electrochim. Acta*, 2002, **48**, 205.
20 I. Kelly, J. Owen and B. Steele, *J. Electroanal. Chem.*, 1984, **168**, 467.
21 R. He and T. Kyu, *Macromolecules*, 2016, **49**, 5637.
22 L.-Z. Fan and J. Maier, *Electrochem. Commun.*, 2006, **8**, 1753.
23 M. Echeverri, N. Kim and T. Kyu, *Macromolecules*, 2012, **45**, 6068.
24 H. de Vries, S. Jeong and S. Passerini, *RSC Adv.*, 2015, **5**, 13598.
25 D. Shang, J. Fu, Q. Lu, L. Chen, J. Yin, X. Dong, Y. Xu, R. Jia, S. Yuan, Y. Chen and W. Deng, *Solid State Ionics*, 2018, **319**, 247.
26 Y.-J. Li, C.-Y. Fan, J.-P. Zhang and X.-L. Wu, *Dalton Trans.*, 2018, **47**, 14932.
27 C. Tao, M.-H. Gao, B.-H. Yin, B. Li, Y.-P. Huang, G. Xu and J.-J. Bao, *Electrochim. Acta*, 2017, **257**, 31.
28 A. M. Rocco, C. P. da Fonseca and R. P. Pereira, *Polymer*, 2002, **43**, 3601.
29 T. Niitani, M. Shimada, K. Kawamura, K. Dokko, Y.-H. Rho and K. Kanamura, *Electrochem. Solid-State Lett.*, 2005, **8**, A385.
30 D. Devaux, D. Glé, T. N. Phan, D. Gigmes, E. Giroud, M. Deschamps, R. Denoyel and R. Bouchet, *Chem. Mater.*, 2015, **27**, 4682.
31 M. A. B. Meador, V. A. Cubon, D. A. Scheiman and W. R. Bennett, *Chem. Mater.*, 2003, **15**, 3018.
32 N. Hasan, M. Pulst, M. H. Samiullah and J. Kressler, *J. Polym. Sci., Part B: Polym. Phys.*, 2019, **57**, 21.
33 M. S. Grewal, M. Tanaka and H. Kawakami, *Electrochim. Acta*, 2019, **307**, 148.
34 W. Wei, Z. Xu, L. Xu, X. Zhang, H. Xiong and J. Yang, *ACS Appl. Energy Mater.*, 2018, **1**, 6769.
35 Y. Jiang, X. Yan, Z. Ma, P. Mei, W. Xiao, Q. You and Y. Zhang, *Polymers*, 2018, **10**, 1237.
36 S.-T. Hsu, B. T. Tran, R. Subramani, H. T. Nguyen, A. Rajamani, M.-Y. Lee, S.-S. Hou, Y.-L. Lee and H. Teng, *J. Power Sources*, 2020, **449**, 227518.
37 H. Zhang, S. Kulkarni and S. L. Wunder, *J. Phys. Chem. B*, 2007, **111**, 3583.
38 Q. Pan, D. M. Smith, H. Qi, S. Wang and C. Y. Li, *Adv. Mater.*, 2015, **27**, 5995.
39 W. Shang, C. Niu, G. Chen, Y. Chen and J. Du, *Electrochim. Acta*, 2020, **338**, 135902.
40 C. Zuo, B. Zhou, Y. H. Jo, S. Li, G. Chen, S. Li, W. Luo, D. He, X. Zhou and Z. Xue, *Polym. Chem.*, 2020, **11**, 2732.
41 S.-H. Wang, S.-S. Hou, P.-L. Kuo and H. Teng, *ACS Appl. Mater. Interfaces*, 2013, **5**, 8477.

42 V. Fleury, J.-N. Chazalviel and M. Rosso, *Phys. Rev. E*, 1993, **48**, 1279.

43 C. Léger, J. Elezgaray and F. Argoul, *Phys. Rev. E*, 1998, **58**, 7700.

44 C.-Z. Zhao, X.-Q. Zhang, X.-B. Cheng, R. Zhang, R. Xu, P.-Y. Chen, H.-J. Peng, J.-Q. Huang and Q. Zhang, *Proc. Natl. Acad. Sci. U. S. A.*, 2017, **114**, 11069.

45 J.-H. Han, E. Khoo, P. Bai and M. Z. Bazant, *Sci. Rep.*, 2014, **4**, 1.

46 P. Bai, J. Li, F. R. Brushett and M. Z. Bazant, *Energy Environ. Sci.*, 2016, **9**, 3221.

47 V. Fleury, M. Rosso, J.-N. Chazalviel and B. Sapoval, *Phys. Rev. A*, 1991, **44**, 6693.

48 J.-N. Chazalviel, *Phys. Rev. A*, 1990, **42**, 7355.

49 Z. Tu, P. Nath, Y. Lu, M. D. Tikekar and L. A. Archer, *Acc. Chem. Res.*, 2015, **48**, 2947.

50 M. Z. Bazant, *Phys. Rev. E*, 1995, **52**, 1903.

51 S. Abbrent, J. Plestil, D. Hlavata, J. Lindgren, J. Tegenfeldt and Å. Wendsjö, *Polymer*, 2001, **42**, 1407.

52 A. Ahmad, U. Farooqui and N. Hamid, *Polymer*, 2018, **142**, 330.

53 R. Miao, B. Liu, Z. Zhu, Y. Liu, J. Li, X. Wang and Q. Li, *J. Power Sources*, 2008, **184**, 420.

54 H. Xie, Z. Tang, Z. Li, Y. He, Y. Liu and H. Wang, *J. Solid State Electrochem.*, 2008, **12**, 1497.

55 L. Li, M. Wang, J. Wang, F. Ye, S. Wang, Y. Xu, J. Liu, G. Xu, Y. Zhang, Y. Zhang, C. Yan, N. V. Medhekar, M. Liu and Y. Zhang, *J. Mater. Chem. A*, 2020, **8**, 8033.

56 M. D. Tikekar, S. Choudhury, Z. Tu and L. A. Archer, *Nat. Energy*, 2016, **1**, 1.

57 C. Monroe and J. Newman, *J. Electrochem. Soc.*, 2005, **152**, A396.

58 G. Yang, C. Chanthad, H. Oh, I. A. Ayhan and Q. Wang, *J. Mater. Chem. A*, 2017, **5**, 18012.

59 M. Herstedt, M. Smirnov, P. Johansson, M. Chami, J. Grondin, L. Servant and J. Lassegues, *J. Raman Spectrosc.*, 2005, **36**, 762.

60 S. Duluard, J. Grondin, J. L. Bruneel, I. Pianet, A. Grélard, G. Campet, M. H. Delville and J. C. Lassègues, *J. Raman Spectrosc.*, 2008, **39**, 627.

61 A. Martinelli, A. Matic, P. Johansson, P. Jacobsson, L. Börjesson, A. Fernicola, S. Panero, B. Scrosati and H. Ohno, *J. Raman Spectrosc.*, 2011, **42**, 522.

62 Q. Lu, J. Fu, L. Chen, D. Shang, M. Li, Y. Xu, R. Jia, S. Yuan and L. Shi, *J. Power Sources*, 2019, **414**, 31.

63 P. R. Chinnam and S. L. Wunder, *Chem. Mater.*, 2011, **23**, 5111.

64 C. M. Costa, M. M. Silva and S. Lanceros-Méndez, *RSC Adv.*, 2013, **3**, 11404.

65 B. K. Wheatle, J. R. Keith, S. Mogurampelly, N. A. Lynd and V. Ganesan, *ACS Macro Lett.*, 2017, **6**, 1362.

66 F. Capitani, F. Trequattrini, O. Palumbo, A. Paolone and P. Postorino, *J. Phys. Chem. B*, 2016, **120**, 2921.

67 M. A. Ratner and D. F. Shriver, *Chem. Rev.*, 1988, **88**, 109.

68 S. Chung, K. Such, W. Wieczorek and J. Stevens, *J. Polym. Sci., Part B: Polym. Phys.*, 1994, **32**, 2733.

69 K. M. Diederichsen, H. G. Buss and B. D. McCloskey, *Macromolecules*, 2017, **50**, 3831.

70 D. M. Pesko, Y. Jung, A. L. Hasan, M. A. Webb, G. W. Coates, T. F. Miller III and N. P. Balsara, *Solid State Ionics*, 2016, **289**, 118.

71 S. B. Aziz, M. Faraj and O. G. Abdullah, *Sci. Rep.*, 2018, **8**, 1.

72 A. Arya and A. Sharma, *Ionics*, 2017, **23**, 497.

73 M. Unge, H. Gudla, C. Zhang and D. Brandell, *Phys. Chem. Chem. Phys.*, 2020, **22**, 7680.

74 M. F. Lagadec, R. Zahn and V. Wood, *Nat. Energy*, 2019, **4**, 16.

75 S. Zugmann, M. Fleischmann, M. Amereller, R. M. Gschwind, H. D. Wiemhöfer and H. J. Gores, *Electrochim. Acta*, 2011, **56**, 3926.

76 F. Han, Y. Zhu, X. He, Y. Mo and C. Wang, *Adv. Energy Mater.*, 2016, **6**, 1501590.

77 K. Xu, *Chem. Rev.*, 2004, **104**, 4303.

78 H. Zhang, F. Chen, O. Lakuntza, U. Oteo, L. Qiao, M. Martinez-Ibañez, H. Zhu, J. Carrasco, M. Forsyth and M. Armand, *Angew. Chem.*, 2019, **131**, 12198.

79 K. Xu, *Chem. Rev.*, 2014, **114**, 11503.

80 G. Homann, L. Stolz, J. Nair, I. C. Laskovic, M. Winter and J. Kasnatscheew, *Sci. Rep.*, 2020, **10**, 1.

81 X. Yang, M. Jiang, X. Gao, D. Bao, Q. Sun, N. Holmes, H. Duan, S. Mukherjee, K. Adair, C. Zhao, J. Liang, W. Li, J. Li, Y. Liu, H. Huang, L. Zhang, S. Lu, Q. Lu, R. Li, C. V. Singh and X. Sun, *Energy Environ. Sci.*, 2020, **13**, 1318.

82 Y. H. Jo, S. Li, C. Zuo, Y. Zhang, H. Gan, S. Li, L. Yu, D. He, X. Xie and Z. Xue, *Macromolecules*, 2020, **53**, 1024.

83 Y. He, S. Chen, L. Nie, Z. Sun, X. Wu and W. Liu, *Nano Lett.*, 2020, **20**, 7136.

84 Z. Wei, Y. Ren, M. Wang, J. He, W. Huo and H. Tang, *Nanoscale Res. Lett.*, 2020, **15**, 1.

85 S. S. Zhang, *J. Power Sources*, 2006, **161**, 1385.